

Experimental Studies of Spray Evaporation in Turbulent Flow

M. Sommerfeld, and H.-H. Qiu*

**Institut für Mechanische Verfahrenstechnik und Umweltschutztechnik
Martin-Luther-Universität Halle-Wittenberg
06099 Halle (Saale), Germany**

*** Department of Mechanical Engineering
Hongkong University of Technology
Honkong**

Abstract

A number of processes in chemical industry and in combustion science involve the evaporation of atomised liquids in a turbulent environment. In order to allow an optimisation of such processes and to provide data for the validation of numerical calculations, the spray evaporation in a heated turbulent air stream was studied experimentally. The flow configuration was a pipe expansion with an expansion ratio of three, where heated air entered through an annulus with the hollow cone spray nozzle being mounted in the centre. In the experiments isopropyl-alcohol was used as a liquid due to its high evaporation rates. Measurements were taken for different flow conditions, such as air flow rate, air temperature, and liquid flow rate in order to provide a set of reliable data. Phase-Doppler anemometry (PDA) was applied to obtain the spatial change of the droplet size spectrum in the flow field and to measure droplet size-velocity correlations. From these local measurements profiles of droplet mean velocities, velocity fluctuations, and droplet mean diameters were obtained by averaging over all droplet size classes. Moreover, recent extensions of the PDA signal processing allowed to determine accurately profiles of the droplet mass flux, wherefrom also the global evaporation rates could be determined. The data for the different flow conditions also include the inlet conditions for air flow and spray (i.e. for all three velocity components),

inlet temperature and wall temperature profiles. The latter was measured using a thermocouple with a special wall sensor.

Introduction

The evaporation of spray droplets in a turbulent environment is of importance for a number of technical and industrial processes. One of the most common processes is the atomisation, evaporation, and combustion of liquid fuels in internal combustion engines and liquid fuelled burners. In the chemical and process engineering industry, for example, a number of products are produced by spray drying (e.g. coffee and washing powders). Other processes involving liquid sprays are spray cooling of surfaces, sprays in wet scrubbers and spray painting.

The two-phase flow in a spray involves a number of complicated physical phenomena. One may identify four flow domains in a spray, where specific physical phenomena are governing the flow:

1. disintegration of a liquid sheet or jet into droplets,
2. dense spray region where interactions between the droplets are prevailing (e.g. coalescence),
3. dilute spray region where the aerodynamic transport of the droplets is dominant,
4. interaction of droplets with rigid walls where either deposition, complete reflection or secondary atomisation (i.e. break-up of one droplet into a number of smaller droplets) take place.

Furthermore, evaporation of droplets in sprays is of importance for a number of applications. The present paper reports a detailed experimental investigation of spray evaporation in a turbulent flow.

As a result of the difficulties involved in performing reliable experiments on sprays evaporating in a heated gas flow under well defined conditions such studies are rare. The evaporation of a Freon-11 spray injected into still air was studied by Solomon et al. (1985) by using rather old fashioned instrumentation. For droplet concentration measurements, isokinetic sampling was used, and the droplet size distribution was determined by photographic and impaction methods. Furthermore, inlet conditions were only obtained farther downstream of the nozzle, and no correlations between droplet size and velocity were given. For detailed numerical predictions of sprays, however, either the break-up has to be modelled or the correlations between drop size and velocity are required at some distance downstream of the nozzle.

A more detailed study of a non-evaporating spray interacting with a co-flowing turbulent air stream was performed by Rudoff et al. (1987) using phase-Doppler anemometry. The measurements include local droplet size distributions and size-velocity correlations. For a number of flow conditions profiles of gas and particle velocities and the Sauter mean diameter were presented.

Experimental studies of a vaporising spray issuing into a co-flowing turbulent air stream were performed by Hanson (1952) and Yule et al. (1983). In the experiments of Hanson (1952), the effect of air stream turbulence on the droplet evaporation was studied where the liquid mass flux downstream of the spray nozzle was obtained by using a rack of collector tubes. Drop sizes and size distributions were measured by a photographic method. The experiments indicated that the turbulence intensity of the flow does not considerably affect the droplet mean diameters, but the size distributions become wider with increasing flow turbulence. Similar findings were obtained in the numerical study of Berlemont et al. (1991), where the Eulerian/Lagrangian approach was used to calculate droplet evaporation in grid turbulence.

The experimental studies of Yule et al. (1983) were mainly focused on the development and testing of an laser-Doppler anemometer with top-hat intensity profile in the probe volume for measurements of the droplet size distribution and the correlations between size and velocity in evaporating kerosene sprays issuing into a co-flowing heated air stream. Results were presented on droplet size distributions, profiles of droplet mean sizes, and correlations between droplet size and velocity.

More recently McDonell and Samuelsen (1995) provided a detailed data base of reacting and non-reacting methanol sprays using different atomisers. The measurements were performed using phase-Doppler anemometry. Maps of the velocity field of spray droplets and gas and the evolution of the Sauter mean diameter were provided and the correlations between droplet size and mean velocity were discussed in detail.

The present study aims to provide detailed experiments on evaporating sprays, including measurements of the inlet conditions, of a spray issuing into a co-flowing heated air stream in order to allow the validation of numerical predictions. Different flow conditions with varying air and liquid flow rates and air temperatures were considered. Measurements were performed using phase-Doppler anemometry, which allows the local droplet size distributions, correlations between droplet size, and velocity, and droplet mass fluxes to be determined.

Experimental Methods

In order to provide appropriate experimental data for the validation of numerical calculations, a test facility which allows measurements with well-defined boundary conditions was built (Fig. 1). The main components of the test facility are a variable speed blower, an electric heater with variable power, a test section, a high pressure vessel for liquid supply, and a cooling trap for recovering the test liquid. The heated air was blown from an

annular injection tube into the test section which had an inner diameter of 200 mm and a length of 1.5 m. With a 64 mm outer diameter of the annulus, an expansion ratio of about 3 was established. The test section was made from an aluminium alloy pipe. In order to allow optical access, several windows using glass plates of 100 μm thickness were mounted along the test section. These thin glass windows resulted in a negligible beam refraction and distortion for the phase-Doppler measurements.

A hollow-cone pressure atomiser was mounted in the cylindrical centre-body of the inlet tube. The diameter, d , of the cylindrical rod was initially 40 mm and in a later stage was changed to 20 mm. The cylindrical rod had a length of 500 mm and was fixed in the inlet tube using perforated rings made of aluminium. By changing the size of the holes in these Plexiglas rings, the flow turbulence level at the inlet could be varied. Liquid isopropyl alcohol was supplied through the centre-body from a pressurised vessel.

The measurements were performed using a one-component phase-Doppler anemometer (PDA), which was mounted on a three-dimensional traversing system with stepper motors in order to allow a computer controlled traversing of the PDA. Measurement of all three velocity components were possible by mounting the PDA-receiver at different positions. The transmitting optics consists of a He-Ne-laser and a conventional one-component LDA-optics with two Bragg cells for frequency shifting (Fig. 2 (a)). The beam separation was 30 mm and a transmission lens with 465 mm focal length was used. The receiving optics was a custom-made module with two photo detectors (i.e. Avalanche photo-diodes). In order to ensure high scattering intensities even for very small droplets, the receiving optics module was positioned at 30° off-axis from the forward scattering direction. The collimating lens of the receiving optics module with a focal length of 310 mm produced a parallel beam of the scattered light, which was partially blocked by two rectangular slits with a height of 10 mm, a width of 60 mm, and a separation of 20 mm (Fig. 2 (a)). A second lens focused the two light rays onto

a common slit having a width of 100 μm (due to the higher droplet concentration at the inlet a 50 μm slit was used to produce a smaller probe volume) which was perpendicular to the slits in the mask and allows demarcation of the measuring volume. The two light beams were focused onto two avalanche-photo-diodes which were integrated into the receiving optics module. All dimensions and characteristics of the PDA optical system are summarised in Table 1. Further details of the PDA system may be found in Qiu and Sommerfeld (1992).

Signal processing was based on a newly developed FFT-processor, involving a number of features which were especially designed to allow accurate droplet concentration and mass flux measurements. The main components of the processor were the real-time SNR (signal-to-noise ratio) Doppler burst detector which produced the trigger signal to initiate data acquisition, an electronic circuit which allowed the Doppler burst peak detection and envelope integration, an A/D converter, and the FFT processor (Fig. 2 (b)). The burst detector was based on the continuous, real-time estimation of the SNR (signal-to-noise ratio) of the band-pass filtered signals from the photo-detectors using a frequency modulation technique (Aizu et al. 1994, Qiu et al. 1994). Furthermore, the magnitude (i.e. amplitude) of one of the signals was evaluated in real-time using a narrow band pass filter, where the bandwidth was only determined by the signal envelope and not by the signal frequency and synchro detector. This resulted in a noise reduction of about 10 dB. A Doppler-signal was only transferred for further processing, i.e. signal frequency and phase estimation using the cross-spectral density (CSD) method in connection with a fast Fourier transform (FFT), when the SNR was above a pre-set lower level. This minimum-SNR could be specified according to the required accuracy for frequency and phase estimation which strongly depends on the SNR (Qiu et al. 1991). The Doppler burst peak detector allowed identification of the maximum in the envelope of the Doppler signal, whereby it was possible to use only this centre portion of the Doppler signal for further signal processing. The integration circuit was used to determine the

integral value under the envelope of the Doppler signal, which allowed estimation of the instantaneous particle velocity vector through the measurement volume which was the basis for accurate particle flux measurements.

The input signals (i.e. the band-pass filtered signals from the two APD's) for the FFT processor were continuously digitised using two A/D converters. The maximum digitising frequency was 20 MHz. The ring memory technique was used to buffer the signals. The burst and peak detector signals were used to control the read-out procedure, which insured that only the centre parts of the Doppler bursts were transferred to the FFT processor. The FFT-processor was based on a hardware FFT chip which calculated the FFT for both channels simultaneously. The maximum clock frequency of the FFT chip was 36 MHz, which resulted in a maximum processing speed of 100 KHz for two channels. For each channel the complex values of the five points near the spectral peak were stored in a buffer memory for up to 1,000 Doppler signals and then transferred to a computer. For the estimation of signal frequency and phase, the five-point interpolation method was applied (Qiu et al. 1991).

For additional validation of the sampled data and to ensure, that the Doppler signals from both channels originate from the same particle or droplet, the maximum amplitude and the frequency of both signals were allowed to only deviate to a certain degree. It should be noted that already the frequency modulation procedure implies a frequency validation. Since the SNR determined by the FFT processor was more accurate than the estimation by the SNR burst detector, an additional software SNR validation was applied. The present measurements were performed with a FFT length of 64 samples and a minimum SNR level of 0 dB was applied at the SNR burst detector and for validation. In all the measurements the statistical bias with respect to the particle size dependent cross-section of the measurement volume (i.e. the probability of detecting large particles is higher than for detecting small particles) was

corrected using the logarithmic mean amplitude method (LMA-method, Qiu and Sommerfeld 1992).

Furthermore, in order to reduce trajectory dependent sizing errors, which may considerably affect the accuracy of the size measurement for a Gaussian beam (Sankar and Bachalo 1991, Grehan et al. 1992), a correlation between particle size and amplitude was used as a validation criterion whereby low amplitude signals from large particles were rejected (Qiu and Sommerfeld 1993).

Accurate measurements of the local droplet concentration or the mass flux in any desired direction in evaporating sprays are essential for the characterisation of the global evaporation rate along the test section. Therefore, a reliable method was developed which allows such measurements when using a one-component PDA-system (Qiu and Sommerfeld 1992, Sommerfeld and Qiu 1995).

The droplet concentration is defined as the number of droplets per unit volume. For a single particle counting instrument, such as a PDA-system, the contribution of each particle crossing the measurement volume to the local concentration was obtained by determining the volume which was swept with the particle across the probe volume during the sampling time Δt_s . This volume is additionally correlated with the particle size- and trajectory-dependent cross-section of the measurement volume $A(\alpha_p, D_p)$ and the magnitude of the instantaneous particle velocity vector $|\vec{U}_p|$:

$$\text{Vol} = |\vec{U}_p| A(\alpha_p, D_p) \Delta t_s \quad (1)$$

The cross-section of the measurement volume does not only depend on the particle or droplet size but also on the direction of particle motion, i.e. $A(\alpha_p, D_p)$ needs to be perpendicular to the direction of particle motion (Sommerfeld and Qiu 1994). The particle mass con-

centration for an ensemble of particles in a complex flow is therefore determined by the following generally valid equation:

$$C_n = \frac{\pi}{6} \frac{\rho_p}{\Delta t_s} \sum_{k=1}^M \left(\sum_{i=1}^{N_k} \frac{D_i^3}{A(\alpha_k, D_i)} \sum_{j=1}^{N_i} \frac{1}{|\bar{U}(D_i)_{kj}|} \right) \quad (2)$$

The summations in Eq. 2 are related to the individual samples (velocity index j), particle size classes (index i), and pre-defined directional classes (index k) and consider the dependence of the particle concentration on the different parameters involved. Therefore, accurate particle concentration measurements require the determination of the instantaneous particle velocity, the particle size and the direction of particle motion through the probe volume. The application of PDA implies that the size of spherical particles can be determined. The particle-size-dependent cross-section of the measurement volume was estimated using the LMA-method introduced by Qiu and Sommerfeld (1992). For the estimation of the instantaneous particle velocity vector with a one-component PDA-system, a method was developed which uses the dependence of the area under the envelope of the band-pass filtered Doppler signal on the particle velocity and the trajectory of the particle through the measurement volume. The integral value for one particle is obtained from:

$$\text{Int}_{kij} = \frac{1}{|\bar{U}(D_i)_{kj}|} \int_0^{s_j} V_{kj}(D_i, x, y, z) ds \quad (3)$$

where $V_{kj}(D_i, x, y, z)$ is the particle size and trajectory dependent Doppler signal envelope and s indicates the particle path through the measurement volume. The summation of all integral values in one directional class for a given size class implies the integration over the cross-section of the measurement volume and gives the following integral value:

$$\text{INT}_{\text{ki}} = \frac{1}{A(D_i)_k} \left[\sum_{j=1}^{N_i} \frac{1}{|\vec{U}(D_i)_{kj}|} \right] \iiint_{\text{Vol}(D_i)} V(D_i, x, y, z) dv \quad (4)$$

By introducing the definition for the particle concentration the following result is obtained:

$$\text{INT}_{\text{ki}} = C_n(D_i)_k \Delta t_s \iiint_{\text{Vol}(D_i)} V(D_i, x, y, z) dv \quad (5)$$

The summation of all the integral values for all the directional classes in one size class yields:

$$\text{INT}(D_i) = \Delta t_s \left[\sum_{k=1}^M C_n(D_i)_k \right] \iiint_{\text{Vol}(D_i)} V(D_i, x, y, z) dv \quad (6)$$

By summing up also the contributions of the individual size classes one finally obtains the particle number concentration as:

$$C_n = \frac{1}{\Delta t_s} \sum_{i=1}^{N_j} \frac{\text{INT}(D_i)}{\iiint_{\text{Vol}(D_i)} V(D_i, x, y, z) dv} \quad (7)$$

Similarly the particle bulk density is obtained:

$$C_m = \frac{\pi \rho_p}{6 \Delta t_s} \sum_{i=1}^{N_j} \frac{D_i^3 \text{INT}(D_i)}{\iiint_{\text{Vol}(D_i)} V(D_i, x, y, z) dv} \quad (8)$$

In order to determine the droplet mass flux in a considered direction n one has to replace

$$1/|\vec{U}(D_i)_{kj}| \quad \text{by} \quad u_{n,kj}/|\vec{U}(D_i)_{kj}| \quad (9)$$

where $u_{n,kj}$ is the velocity component in the direction of the flux to be measured:

$$F_n = \frac{\pi \rho_p}{6 \Delta t_s} \sum_{i=1}^{N_k} \frac{D_i^3 \sum_{k=1}^M \sum_{j=1}^{N_i} \text{Int}_{kij} u_{n,kj}}{\iiint_{\text{Vol}(D_i)} V(D_i, x, y, z) dV} \quad (10)$$

The accuracy of the above described method was tested in an isothermal spray by Sommerfeld and Qiu (1995). The integration of the measured droplet mass flux profiles provided the liquid mass flow rate along the spray which agreed for the different profiles to $\pm 10\%$ with an independent measurement by weighing the liquid consumption for a given time period.

The procedure for measuring the inlet conditions of the air flow and the spray is described in the following paragraphs. The hollow cone spray nozzle was mounted in such a way that the exit hole was about 5 mm above the edge of the centre-body. This ensured that a complete break-up of the liquid sheet occurs up to the edge of the centre-body. The inlet conditions for the droplet phase, i.e. local size distributions, local size-velocity correlations for all three velocity components and droplet mass fluxes could be measured 3 mm downstream of the edge of the centre-body (this gives a distance of 8 mm downstream of the nozzle exit) in order to provide the required data for numerical calculations. The three components of air velocity at the inlet were also measured 3 mm downstream the edge of the centre-body. For these measurements the spray was not operated. The velocity measurements by PDA were performed by seeding the flow with small spherical glass beads and applying the discrimination procedure described by Qiu et al. (1991) in order to ensure that only signals from small particles with a diameter smaller than $3\text{ }\mu\text{m}$ were sampled. These small particles can be assumed to follow the gas phase turbulent fluctuations.

The mean temperature of the air flow at the inlet was measured with a thermocouple probe scanned across the annulus. In the single phase flow, profiles of the mean temperature in the test section also were measured by this thermocouple probe. Moreover, the outer wall temperature along the test section was measured for all flow conditions using a special wall thermocouple probe. The probe head consisted of metal strips which could be placed flush onto the wall. In the paper only the outer wall temperature is presented. The temperature at

the inner wall may be determined from these values by calculating the heat conduction through the 3 mm thick aluminium wall.

The first flow condition considered in the studies was a single phase flow case (i.e. without the liquid spray being operated, see Table 2) in order to assess the flow characteristics and quality of the established air flow and the effect of the spray and the evaporation on the flow (i.e. two-way coupling).

The two-phase flow was examined for a number of flow conditions with different air flow rates, air temperatures, liquid flow rates, and diameters of the nozzle holder (Sommerfeld et al. 1994). However only four cases are discussed here. The main parameters for the different experimental conditions are summarised in Table 2.

Since the test section could not be insulated due to the required optical access, the droplet evaporation was of course influenced by the ambient temperature. Therefore, the measurements for one flow condition were performed during a relatively short time period (i.e. one or two days) to ensure no considerable changes in the ambient temperature. In order to quantify the errors associated with variations in the ambient temperature, the droplet mass flux was measured at $x = 25$ mm for the flow condition 3 at two ambient temperatures (i.e. 25.4 and 31.4°C). The results are summarised in Fig. 3 and Table 3. It is obvious that the evaporation rate is smaller at lower ambient temperatures and hence lower wall temperatures, whereby the liquid mass flow rate is about 30% higher compared to the higher ambient temperature. This implies an error in the measured liquid mass flow rate of 5 % per one degree Celsius of ambient temperature change. Therefore, a maximum variation of only 2°C was allowed for each series of measurements performed.

Measurements in Single Phase Flow

A simultaneous measurement of gas and droplet velocities in the evaporating spray was not possible in the present study for several reasons. As a result of the evaporation the number of naturally occurring small droplets (i.e. droplets with diameters below 3 μm) which are able to follow the turbulent gas-phase fluctuations and hence can serve as an indicator of the gas velocity, was very low. This would result in excessive measurement times to determine the gas velocity. Moreover, the spray droplets are not present in the entire flow field.

The injection of solid tracers in the gas flow would result in a contamination of the windows in the test section and additionally considerably influence the evaporation characteristics due to agglomeration with the spray droplets. The addition of small liquid droplets in the annular air stream, on the other hand, will affect the balance of liquid mass flow, the vapour concentration in the flow field and may also result in coalescence between tracer and spray droplets. Furthermore, small droplets added to the air flow will evaporate very fast, mainly already in the inlet pipe. Hence, addition of larger droplets would be required, which will again considerably alter the vapour mass fraction in the flow field. All the above described problems conflict with the need to specify detailed inlet and boundary conditions of the flow in order to provide data for validating numerical calculations which were performed in parallel to the experimental studies.

Therefore, in order to characterise the established gas flow one set of measurements was taken without the spray in operation. Under such conditions the air flow could be seeded with small spherical glass beads and the air velocity was determined by applying the discrimination procedure described by Qiu et al. (1991) for insuring that only particles smaller than about 3 μm were sampled. For each measurement location 2,000 validated samples were recorded in order to allow a determination of the mean velocities and the rms values with low statistical error.

In Fig. 4 the cross-sectional profiles of the axial and radial mean velocities, the turbulent kinetic energy and the mean temperature of the air flow are summarised. It is obvious that the flow is fairly symmetric. In front of the nozzle holder a small re-circulation region develops and the re-circulation region in the edge of the pipe expansion extends throughout the considered flow domain (Fig. 4 (a)). The highest gas temperatures are found in the core region of the flow field. Within the re-circulation region of the pipe expansion the gas temperature is about 15°C lower due to the wall cooling effect (Fig. 4 (d)). The inner wall temperature was estimated from the measurements of the outer wall temperature along the test section. At $x = 400$ mm an almost uniform gas temperature distribution is established.

Measurements in evaporating spray

The measurements in evaporating sprays include local size distributions, size-velocity correlations and droplet mass flux. For each measurement location 20,000 validated samples were collected for the reliable determination of mean properties. The droplet mean velocities and the mean fluctuating velocities were determined by averaging over the entire droplet size spectrum.

In the following section, the experimental results obtained for the droplet phase in case 2 (see Table 2) are discussed in more detail, since it corresponds to the single phase flow discussed above. A comparison of the wall temperature profiles for the single- and two-phase flow reveals the effect of evaporation (Fig. 5). Due to the heat required for droplet heat-up and evaporation the air flow is cooled and hence the wall temperature for the two-phase case is considerably lower as compared to the single phase flow. Initially, where the evaporation rates are higher (i.e. between $x = 0$ and 400 mm), the difference is about 15°C. Further downstream the difference reduces to about 5°C.

The measured profiles of the axial velocities and the associated velocity fluctuations averaged over all droplet size classes are shown in Fig. 6 for the seven cross-sections considered. The profiles of the axial droplet velocities exhibit a rather symmetric shape which demonstrates the proper alignment of the flow and the spray nozzle. In regions, where no velocity data are plotted, the number density of the droplets was too low to acquire data within a reasonable measuring time. The maximum averaged axial velocity just downstream of the spray nozzle is about 15 m/s and then decreases to about 10 m/s at $x = 25$ mm (Fig. 6 (a)). Moving further downstream ($x = 50$ and 100 mm), a slight increase of the maximum droplet velocity is observed, which is associated with the acceleration of the droplets by the annular air stream. Downstream of $x = 100$ mm, the maximum axial droplet velocity slightly decays resulting from the radial spreading of the spray and the air jet. The re-circulation region developing downstream of the nozzle holder results in negative droplet velocities in the core of the spray (i.e. at $x = 25$ mm).

The radial velocity component could only be measured in one half of the pipe cross-section due to the arrangement of the optical system. The profiles of the radial droplet mean velocity (Fig. 6 (c)) reveal that there exists an inward motion of the droplets in the core region of the spray just downstream of the injection location within the central re-circulation region developing below the cylindrical rod, which was used to hold the spray nozzle (i.e. $x = 25$ and 50 mm). At the edge of the spray, i.e. where the highest liquid mass flux exists, the largest radial velocities are found indicating the outward radial spread of the spray. From the nozzle exit up to $x = 100$ mm the maximum radial velocity continuously decreases and downstream of $x = 100$ mm the radial spread increases again slightly. This behaviour shows that initially air from the annular jet is entrained into the spray causing a reduction in the radial spread. Moving further downstream, the flow continuously expands due to the reducing dimensions of the re-circulation region in the edge of the pipe expansion.

The measured profiles of the droplet number mean diameter show the typical result expected from a hollow-cone atomiser where smaller droplets are found in the core region and larger droplets near the edge of the spray (Fig. 7 (a)). With increasing distance from the inlet, the droplet mean diameter becomes more and more uniform over the pipe cross-section due to evaporation, turbulent dispersion and entrainment from the outer region of the spray. From $x = 300$ mm the number mean droplet diameter is almost constant in the cross-section and slowly decreases with downstream distance as a result of evaporation. The largest changes of the droplet number mean diameter are observed at the edge of the spray where the highest evaporation rates are expected. The profiles of the standard deviations of the local droplet size distributions show, that narrow size distributions are found in the core of the spray while towards the edge, a rapid increase of the standard deviation is observed (Fig. 7 (b)). This is associated with rather wide size distributions. Downstream of $x = 300$ mm the diameter rms-value becomes uniform and is below $10\text{ }\mu\text{m}$. The profiles of the Sauter diameter (Fig. 7 (c)) are similar to those of the number mean diameter but the values are between 5 to $10\text{ }\mu\text{m}$ larger. The differences are smaller in the core of the spray than near the edge.

The distribution of the axial droplet mass flux throughout the test section is shown in Fig. 8. Initially (at $x = 0$ and 25 mm) the profiles of the droplet mass flux show the two peaks associated with a hollow-cone spray nozzle and the spray is spreading according to the cone angle of 60° . Due to the re-circulation region downstream of the centre body, the droplet mass flux becomes negative in the cone of the spray at $x = 25$ mm. Further downstream the spreading of the spray is hindered due to the entrainment of the annular air jet and the maximum of the droplet mass flux moves towards the centreline. Downstream of $x = 50$ mm, the droplet mass flux is continuously decreasing and at $x = 400$ mm most of the liquid has evaporated.

In order to reduce the disturbance of the spray evolution by the re-circulation region developing in front of the nozzle holder and to reduce the strong inward motion of the annular air jet which hinders the radial spread of the spray and hence evaporation, further experiments were conducted with a nozzle holder of 20 mm diameter (case 4 in Table 2). Moreover, the maximum air velocity in the annulus was reduced to 9 m/s, whereby the initial relative velocity between air and droplets is increased and hence the convective contribution to the droplet evaporation should become larger yielding a higher overall evaporation rate. In Fig. 9 the development of the spray for this condition (case 4) is demonstrated using the profiles of the droplet axial and radial mean velocities (Fig. 9), the droplet mass flux (Fig. 10), and the droplet number mean diameter together with the size rms-value (Fig. 11). In comparison to case 2 (Figs. 6 to 8) it is obvious that the radial spread of the spray has increased and the characteristics of the hollow-cone spray are maintained up to 200 mm downstream of the nozzle exit, i.e. the droplet mass flux profiles show two maxima up to this location (Fig. 10).

The comparison of axial mean droplet velocity profiles for both cases shows the reduced size of the re-circulation region downstream of the nozzle holder, i.e. no negative velocities are observed at $x = 25$ mm. Moreover, the lower air injection velocity in case 4 results in considerably lower axial velocities of the spray droplets, except for the first two profiles (Fig. 9 (a)), where the interaction with the annular air flow is weak. These lower droplet velocities compared to case 2 increases the residence time of the droplets within the test section yielding more time for evaporation. The radial mean velocity profiles of the droplet phase (Fig. 9 (b)) reveals that no inward motion in the core of the spray is realised as found in case 2 (Fig. 6 (c)) and that initially a higher radial spread is observed which is also obvious from the mass flux profiles (compare Fig. 8 and Fig. 10). The reduced entrainment of hot air into the spray also has consequences for the evolution of the droplet number mean diameter (Fig.

11). The droplet mean diameter in the core of the spray remains considerably lower (i.e. between 10 and 15 μm) up to $x = 200$ mm compared to case 2, indicating that the flux of larger droplets from the outer region of the spray due to entrainment is reduced for case 4 (compare with case 2, Fig. 7). At the edge of the spray the droplet diameters are similar for case 4 and 2.

The droplet size distributions at selected locations within the region of spray development (i.e. for the profile at $x = 50$ mm) show that in the core of the spray rather narrow size distributions with a low number mean diameter are found (Fig. 12 (a)). Towards the edge of the spray the mean diameter increases and the size distribution is considerably broadened, associated with an increase of the diameter rms-value (Fig. 11 (b)). Moreover, a strong correlation between droplet size and axial velocity exists with the larger droplets having the higher velocities due to their larger inertia (Fig. 12 (b)). Outside the main spray region, in the re-circulation region of the pipe expansion only a few droplets are present (Fig. 10) all of which have negative velocities (Fig. 12 (c) and (d)). The droplet number mean diameter is only slightly decreasing, but the rms-value increases further since a broadening of the size distribution towards smaller droplets is occurring (Fig. 12 (d)). Downstream of $x = 200$ mm the droplet number mean diameter and the associated rms value become more and more constant in the pipe cross-section. At $z = 400$ mm no considerable variation in the droplet size distribution are observed and no correlation between size and axial velocity is existing (Fig. 13).

The overall change in droplet size for the cases 1, 2, and 4 is illustrated by calculating for each profile an average Sauter diameter weighted with the local droplet mass flux (Fig. 14). The larger changes of the mean Sauter diameter just downstream of the nozzle up to $x = 25$ mm are associated with the disturbances caused by the nozzle holder. Further along the spray the averaged Sauter diameter continuously is reduced due to evaporation. The lowest

decrease is observed for case 1 with an air temperature of 80°C. The overall reduction of the averaged Sauter mean diameter within the test section is between 10 and 15 μm .

For a further comparison of the different cases, the profiles of the droplet mass flux were integrated to yield the droplet mass flow rate in the considered cross-sections. The normalised droplet mass flow rates along the test section, plotted in Fig. 15, demonstrate the different evaporation rates for the cases 1, 2 and 4. For case 1, a rather continuous decrease of the droplet mass flow rate is observed and 400 mm downstream of the injection 67 % of the liquid is evaporated. Considering case 2, where an air injection temperature of 100°C was established, the evaporation rate is initially almost identical to that of case 1 and between $x = 50$ and 100 mm the droplet mass flow rate remains almost constant. This might be caused by an asymmetry of the spray due to the interaction with the re-circulation region downstream of the nozzle holder whereby larger errors in the measured droplet mass flow rate may result since this value was determined from the integration of one droplet mass flux profile only. Further downstream, the evaporation rate increases again, and the droplet mass flow rate decreases below that of case 1. Finally, at $x = 400$ mm, 90% of the liquid isopropyl alcohol is evaporated. For case 4 with a maximum air injection velocity of 9 m/s and a temperature of 100°C the overall evaporation rate is considerably higher as compared to the other two cases. The main reason for this is the larger radial spread of the spray, the higher relative velocity between gas and droplets in the initial region downstream of the inlet (i.e. maximum axial air velocity 9 m/s, maximum axial droplet injection velocity 15 m/s) and the larger residence time of the droplets. The higher relative velocity may increase the convective droplet evaporation compared to the other cases. The highest evaporation rate is found between $x = 25$ and 50 mm. At $x = 400$ mm, 99% of the droplet mass is evaporated, hence this flow condition gives the highest overall evaporation rate.

The temperature distribution along the outer wall of the test section reveals that the temperature levels strongly depend on the air inlet temperature and the evaporation rate (Fig. 16). In case 2 the wall temperature is higher compared to case 1 due to the higher air injection temperature. In these two cases the same liquid mass flow rate was established. For case 4 the injected liquid mass flow rate was about twice than that in the other cases. Hence, the lowest wall temperatures are observed in case 4 as a result of the high evaporation rates and the associated cooling of flow and walls. As already mentioned previously, the high evaporation rates in case 4 are caused by the large relative velocity between air and droplets near the injection location and the larger residence time of the droplets. The temperature maximum for all three cases is found near the re-attachment location of the re-circulation region in the pipe expansion, which is located approximately 600 mm downstream of the inlet.

Conclusions

A series of detailed measurements of the droplet phase properties in a spray issuing into a co-flowing heated air stream was collected using phase-Doppler anemometry. The measured quantities include droplet size distributions, correlations between droplet size and velocity and the droplet mass flux at the inlet and within the entire flow field. From the measured droplet mass flux profiles, the liquid mass flow rate along the test section was determined. The results reveal, that low air injection velocities compared to the droplet initial velocity increase the evaporation rate as a result of the larger droplet interaction time with the surrounding heated air and the established larger relative velocity between air and droplets, whereby the convective droplet evaporation is increased. Moreover, the reduction in air injection velocity allows for a larger radial spread of the spray. Higher air temperature also

increase the evaporation rate but are less effective than the reduction in the air injection velocity. Additionally, higher air temperatures require more energy input.

The experimental results presented here, provide all required boundary conditions and data to allow for the validation of numerical calculations of evaporating sprays. The data are available on request.

Acknowledgement

The present studies were performed at the Institute of Fluid Mechanics of the University Erlangen-Nürnberg in the frame of an EC-project (Contract No. JOUE-CT-91-067). The financial support by the European Commission is gratefully acknowledged.

List of References

- Aizu, Y., Domnick, J., Durst, F., Grehan, G., Onofri, F., Qui, H.-H, Sommerfeld, M., Xu, T.-H. and Zieme, M., 1994, A new generation of phase-Doppler instruments for particle velocity, size, and concentration measurements. *Particle and Particle Systems Characterization*, **11**, 43-53.
- Berlemont, A., Grancher, M.-S. and Gouesbet, G., 1991, On the Lagrangian simulation of turbulence influence on droplet evaporation. *Int. J. Heat Mass Transfer*, **34**, 2805-2812.
- Grehan, G., Gouesbet, G., Nagwi, A. and Durst, F., 1992, On elimination of the trajectory effects in phase-Doppler systems. *Proc. 5th European Symp. Particle Characterization (PARTEC 92)*, pp. 309-318.
- Hanson, A. R., 1952, The evaporation of a fuel spray in an airstream and effect of turbulence on droplet size distribution. *Proc. of the 2nd Midwest Conf. on Fluid Mechanics*, 415-428.

- McDonnell, V.G. and Samuelsen, 1995, An experimental data base for the computational fluid dynamics of reacting and nonreacting methanol sprays. *Transactions of the ASME, Journal of Fluids Engineering*, **117**, 145-153.
- Qiu, H.-H., Sommerfeld, M. and Durst, F., 1991, High resolution data processing for phase-Doppler measurements in a complex two-phase flow. *Measurement Science and Technology*, **2**, 455-463.
- Qiu, H.-H. and Sommerfeld, M., 1992, A reliable method for determining the measurement volume size and particle mass fluxes using phase-Doppler anemometry. *Experiments in Fluids*, **13**, 393-404.
- Qiu, H.-H. and Sommerfeld, M., 1993, The impact of signal processing on the accuracy of phase-Doppler measurements", Proc. 6th Workshop on Two-Phase Flow Predictions, Erlangen 1992, (Ed. Sommerfeld, M.), Bilateral Seminars of the International Bureau Forschungszentrum Jülich, 421-430.
- Qiu, H.-H., Sommerfeld, M. and Durst, F., 1994, Two novel Doppler signal detection methods for laser-Doppler and phase-Doppler anemometry. *Measurement Science and Technology*, **5**, 769-778.
- Rudoff, R. C., Houser, M. J. and Bachalo, N. D., 1987, Two-phase Flow measurements of a spray in a turbulent flow. AIAA Paper No. 87-0062.
- Sankar, S.V. and Bachalo, W.D., 1991, Response characteristics of the phase-Doppler particle analyzer for sizing spherical particles larger than the wavelength. *Applied Optics*, **30**, 1487-1496.
- Solomon, A. S. P., Shuen, J.-S., Zhang, Q.-F. and Faeth, G. M., 1985, Measurements and predictions of the structure of evaporating sprays. *J. of Heat Transfer, Transactions of the ASME*, **107**, 679-686.

Sommerfeld, M., Kohnen, G. and Qiu, H.-H., 1994, Advanced flow modelling for industrial applications. Final Report for EC Contract JOUE CT 91-0067.

Sommerfeld, M. and Qiu, H.-H., 1995, Particle concentration measurements by phase-Doppler anemometry in complex dispersed two-phase flows, *Experiments in Fluids*, 18,187-198.

Yule, A. J., Ereaut, P. R. and Ungut A., 1983, Droplet sizes and velocities in vaporizing spray. *Combustion and Flame*, **54**, 15-22.

Tables

<u>Transmitting optics:</u>		
Wave length of the laser	632.8	nm
Diameter of laser beam (D_{e-2})	1.0	mm
Focal length of front lens	485	mm
Beam separation	30	mm
Diameter of measuring volume	391	μm
Length of measuring volume	12.6	mm
Fringe spacing	10.24	μm
Fringe number	38	-
Shift frequency	2	MHz
Conversion factor	10.24	(m/s)/MHz
<u>Receiving optics:</u>		
Off axis angle	30	degree
Focal length of collimating lens	310	mm
Dimensions of rectangular apertures	60 x 10	mm
Detector separation	20	mm
Focal length of imaging lens	160	mm
Width of spatial filter	100	μm
Imaged length of measuring volume	194	μm
Phase conversion factor	1.75	degree/ μm

Table 1 Parameters of the PDA optical system

case	diameter nozzle holder	air volume flow rate	air mass flow rate	maximum air velocity	maximum air temperature	liquid mass flow rate	liquid tem- perature at nozzle exit
(-)	(mm)	(m ³ /s)	(g/s)	(m/s)	(°C)	(g/s)	(°C)
single phase flow	40	0.032	29.0	18.0	100	-	-
1	40	0.034	32.6	18.0	80	0.44	32
2	40	0.031	28.3	18.0	100	0.44	34
3	40	0.015	14.2	9.0	80	0.44	32
4	20	0.023	21.2	9.0	100	0.83	34

Table 2 Flow conditions for the considered measurements

ambient temperature	droplet mass flow rate	percentage
[°C]	[g/s]	[%]
25.4	0.273	130
31.4	0.210	100

Table 3 Droplet mass flow rate at $z = 25$ mm for two ambient temperatures (case 3)

Figure Captions

Fig. 1 Sketch of the test facility and dimensions of the test section (in mm)

Fig. 2 Phase-Doppler anemometer, a) optical system, b) data acquisition

Fig. 3 Influence of ambient temperature on droplet mass flux profiles at $x = 25$ mm (case 3)

Fig. 4 Measurements for the single-phase flow case (see Table 5), a) axial mean velocity, b) axial velocity fluctuation, c) radial mean velocity, d) mean temperature.

Fig. 5 Comparison of wall temperature distribution along the test section for the single- and two-phase flow case

Fig. 6 Measured droplet velocity profiles for case 2 (velocity in m/s), a) axial mean velocity, b) axial velocity fluctuations, c) radial mean velocity

Fig. 7 Profiles of measured droplet number mean diameter (a) and standard deviation of number mean diameter (b) for case 2 (in μm)

Fig. 8 Profiles of measured droplet mass flux for case 2 (in $\text{kg}/(\text{m}^2 \text{ s})$)

Fig. 9 Profiles of measured axial (a) and radial (b) droplet mean velocities (in m/s) for case 4

Fig. 10 Profiles of droplet mass flux (in $\text{kg}/\text{m}^2 \text{ s}$) for case 4

Fig. 11 Profiles of measured droplet number mean diameter (a) and diameter rms-value (b) for case 4 (in μm)

Fig. 12 Droplet size distributions and size-velocity correlations at the cross-section 50 mm downstream the inlet, a) $y = 0$ mm, b) $y = 36$ mm, c) $y = 60$ mm and d) $y = 90$ mm

Fig. 13 Droplet size distributions and size-velocity correlations at the cross-section 400 mm downstream the inlet, a) $y = 0$ mm, b) $y = 50$ mm

Fig. 14 Averaged Sauter diameter along the test section for cases 1, 2, and 4

Fig. 15 Droplet mass flow rate along the test section for cases 1, 2 and 4

Fig. 16 Temperature distribution along the outer wall of the test section for cases 1, 2 and 4

Figures

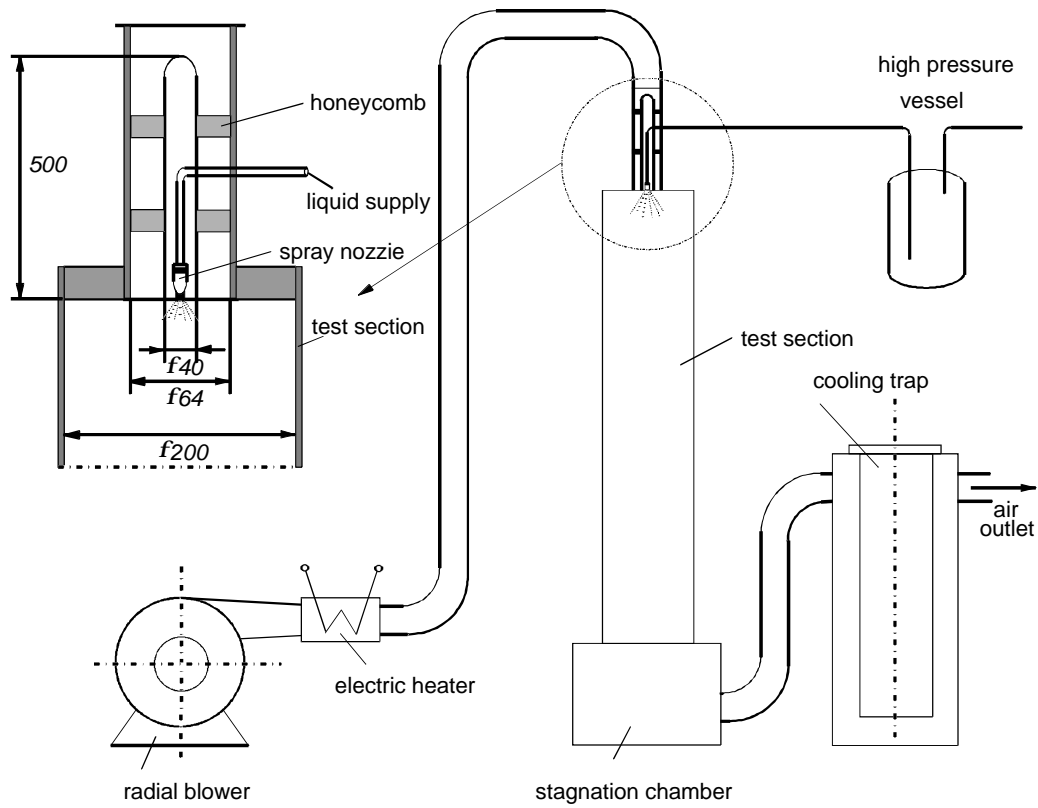


Fig. 1 Sketch of the test facility and dimensions of the test section (in mm)

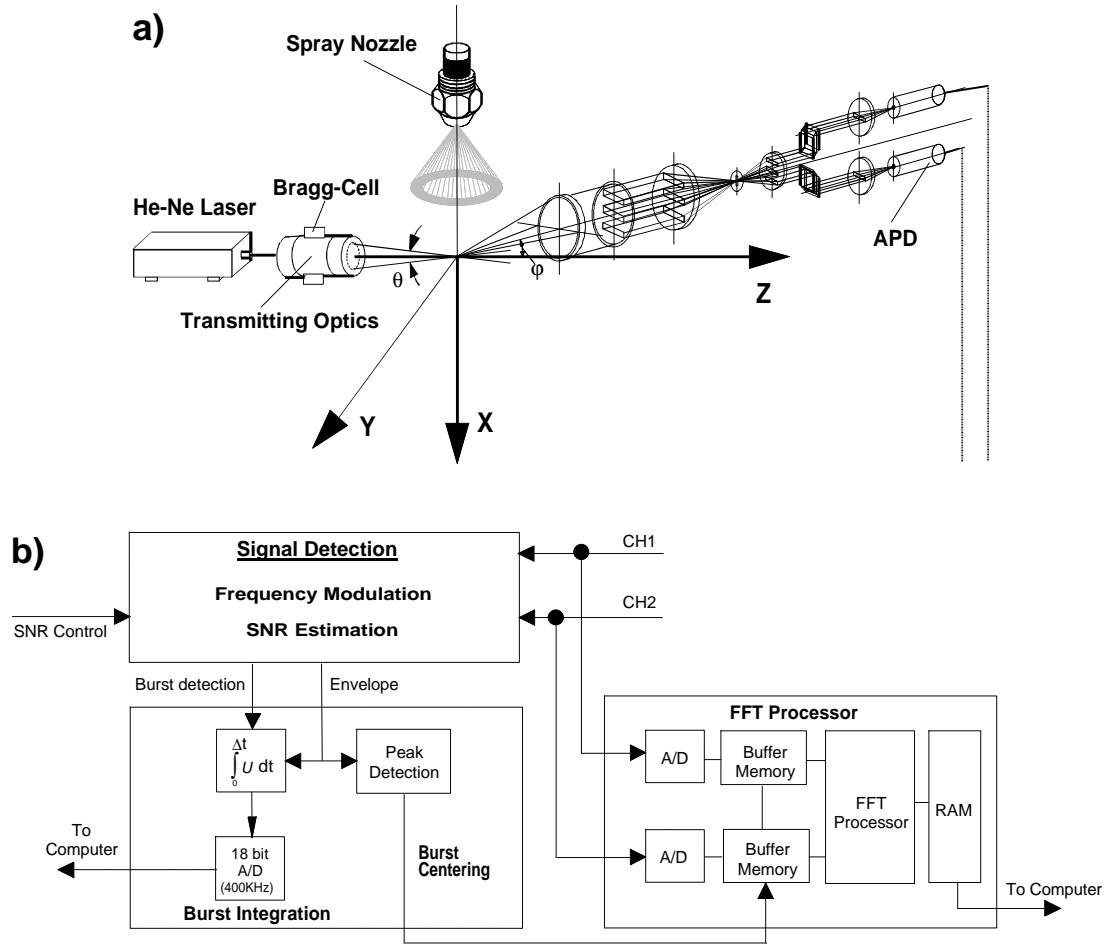


Fig. 2 Phase-Doppler anemometer, a) optical system, b) data acquisition

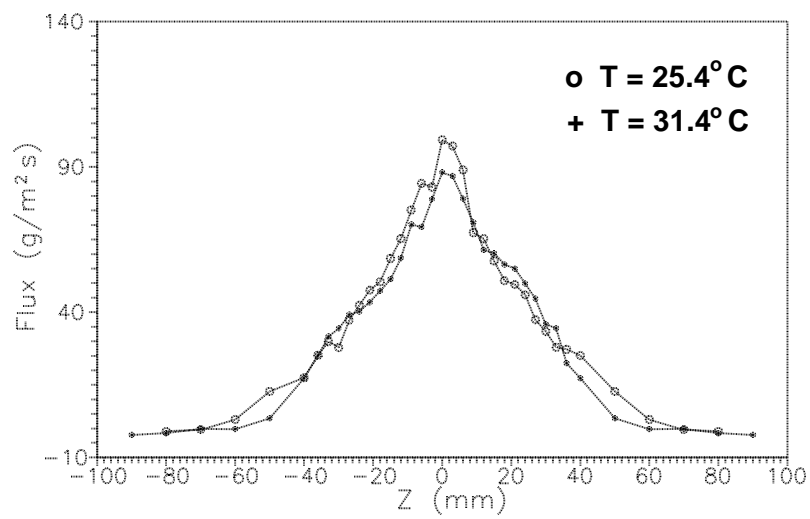


Fig. 3 Influence of ambient temperature on droplet mass flux profiles at $x = 25$ mm (case 3)

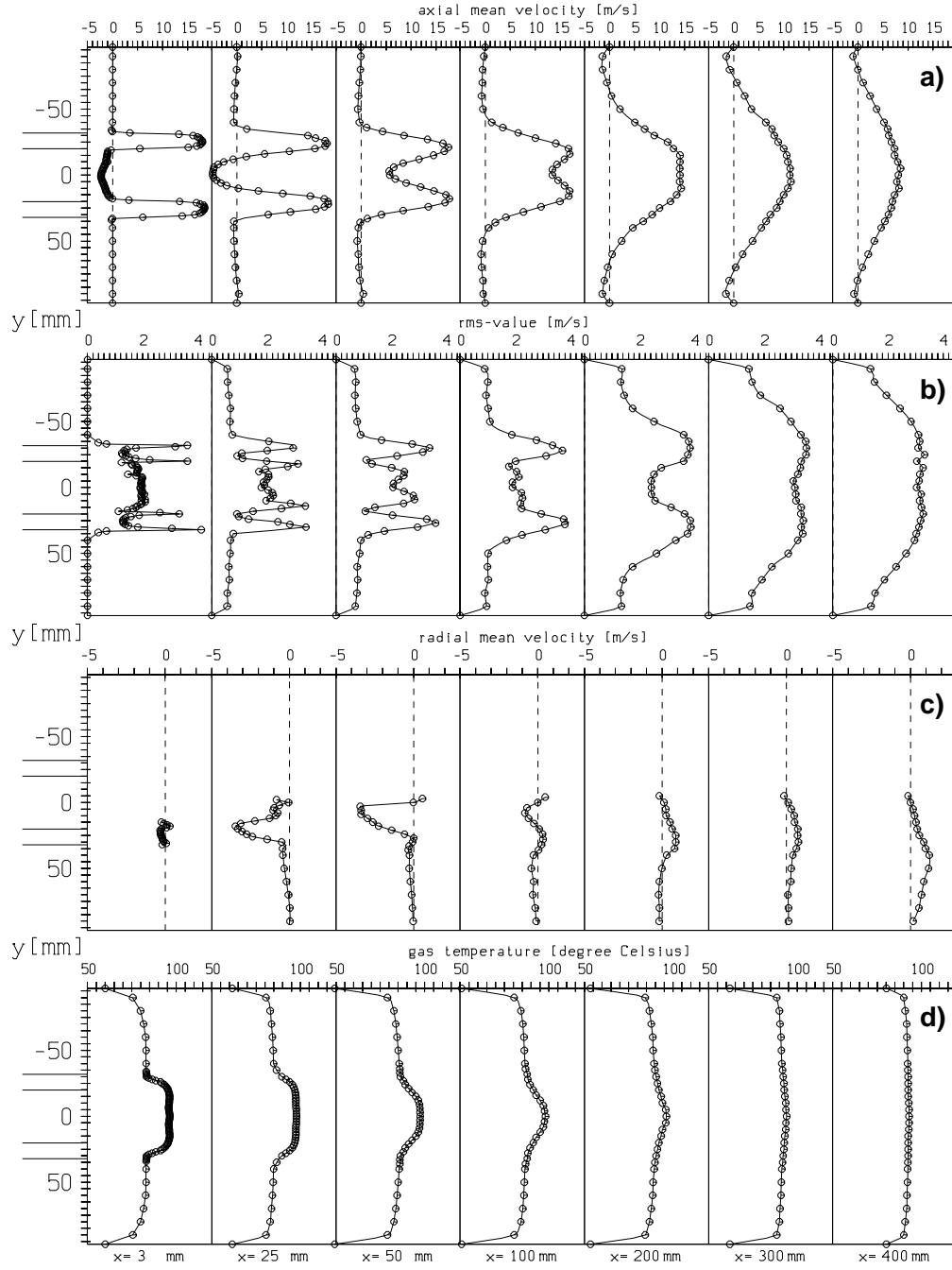


Fig. 4 Measurements for the single-phase flow case (see Table 5), a) axial mean velocity, b) axial velocity fluctuation, c) radial mean velocity, d) mean temperature.

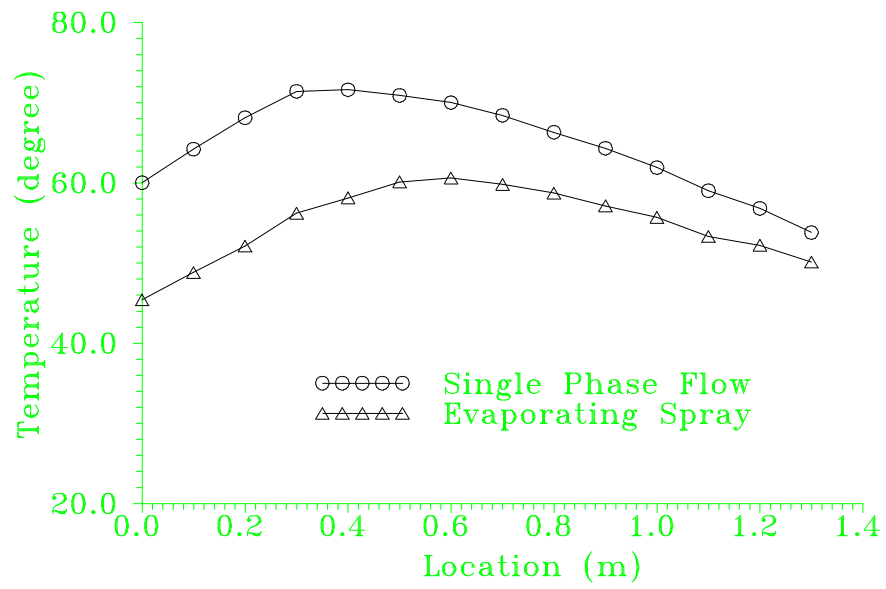


Fig. 5 Comparison of wall temperature distribution along the test section for the single- and two-phase flow case

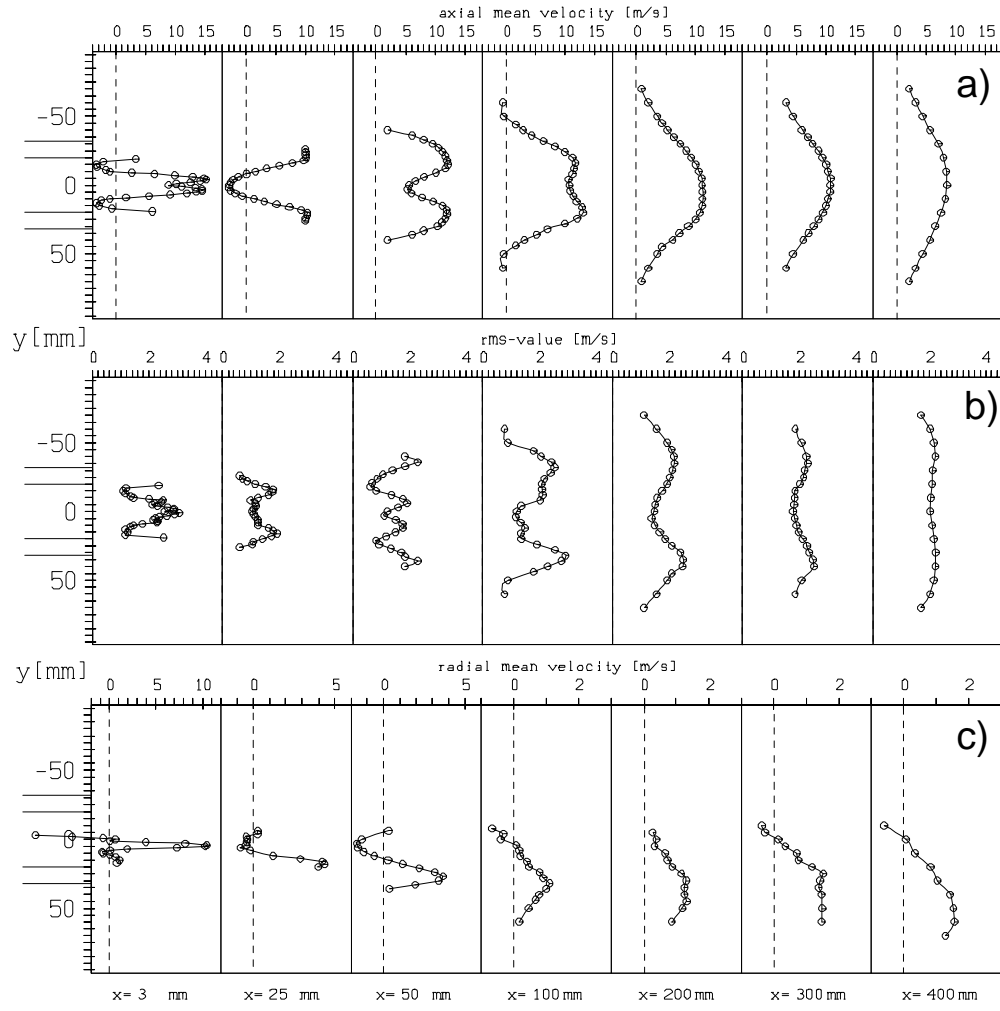


Fig. 6 Measured droplet velocity profiles for case 2 (velocity in m/s), a) axial mean velocity, b) axial velocity fluctuations, c) radial mean velocity

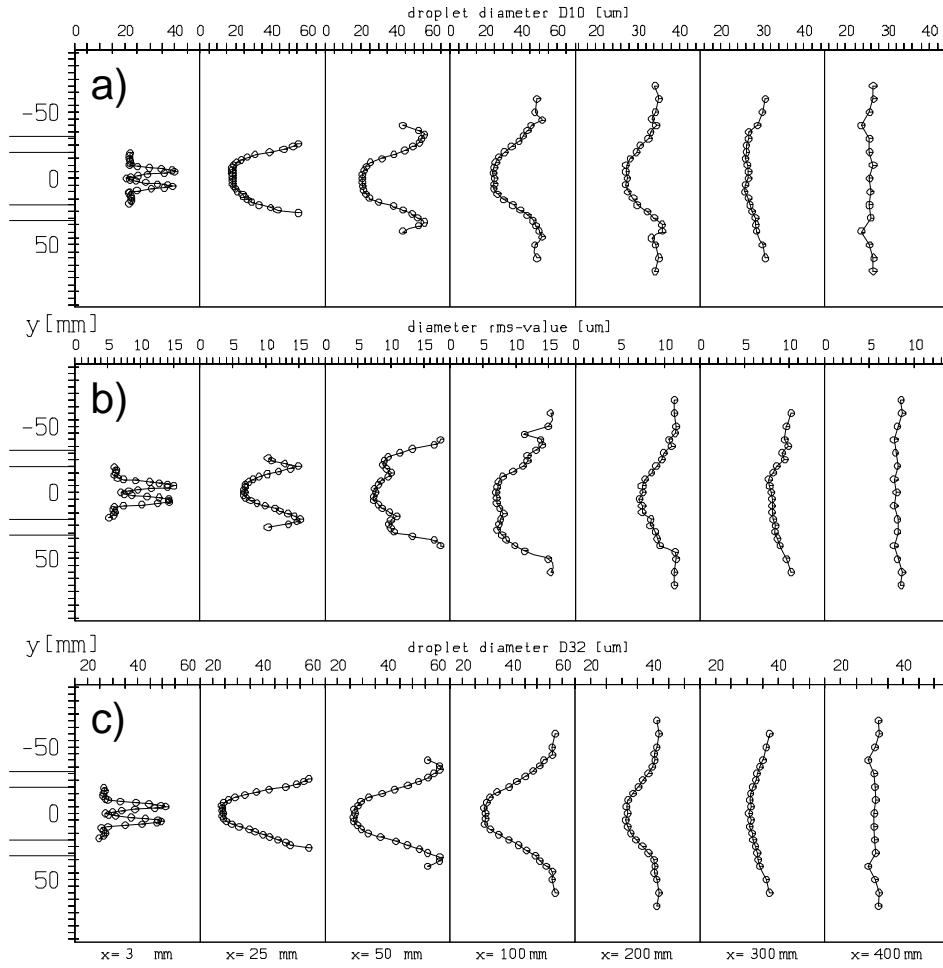


Fig. 7 Profiles of measured droplet number mean diameter (a), standard deviation of number mean diameter (b), and Sauter mean diameter (c) for case 2 (in μm)

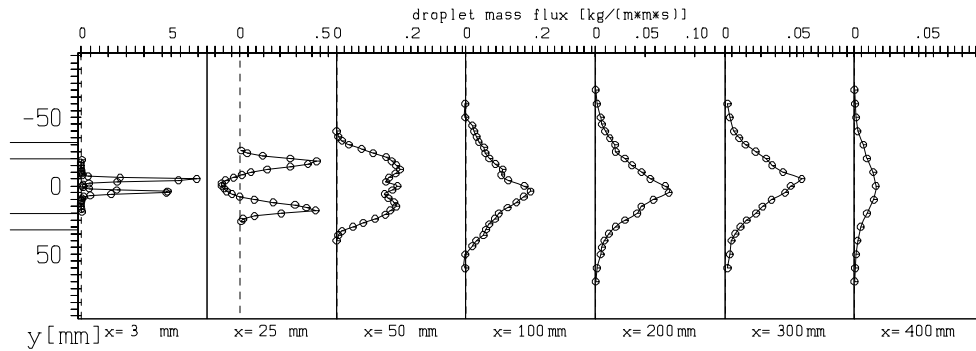


Fig. 8 Profiles of measured droplet mass flux for case 2 (in $\text{kg}/(\text{m}^2 \text{s})$)

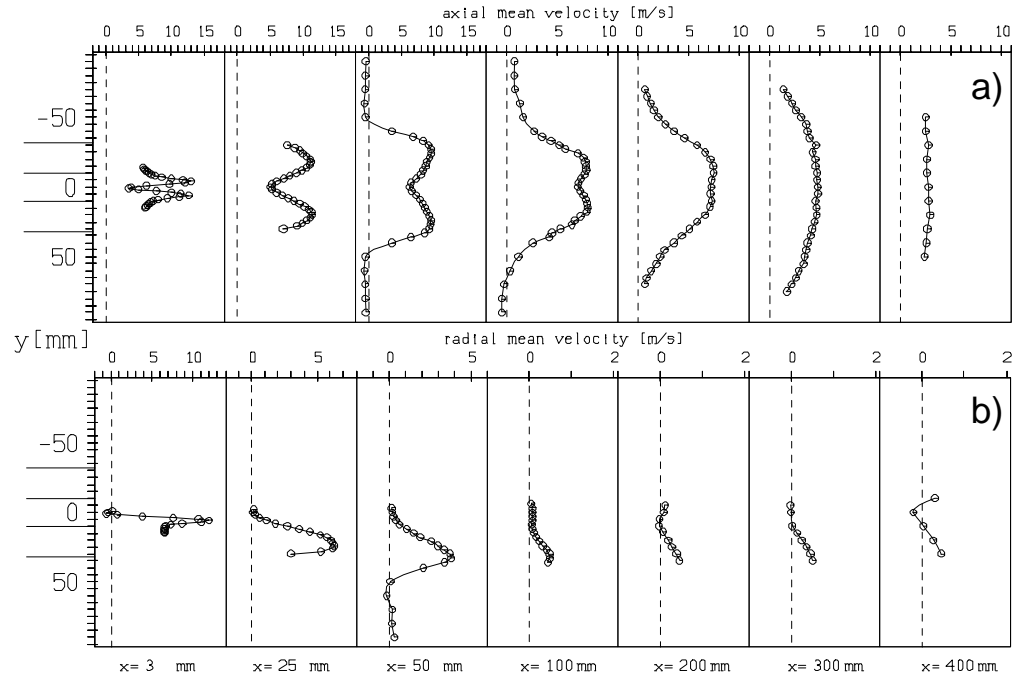


Fig. 9 Profiles of measured axial (a) and radial (b) droplet mean velocities (m/s) for case 4

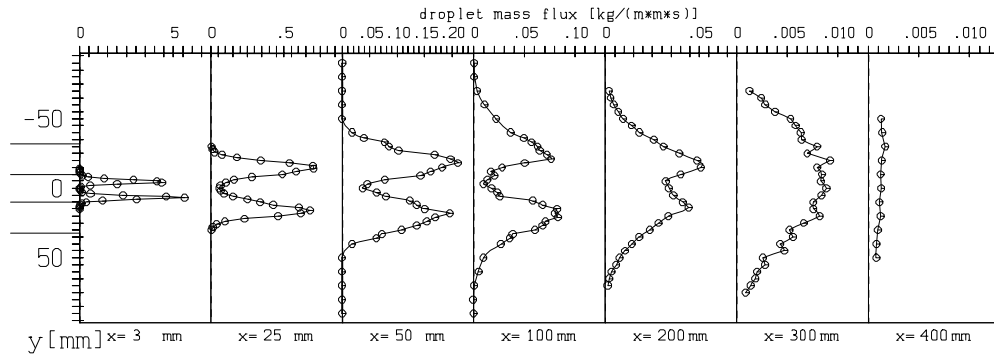


Fig. 10 Profiles of droplet mass flux ($\text{kg/m}^2 \text{s}$) for case 4

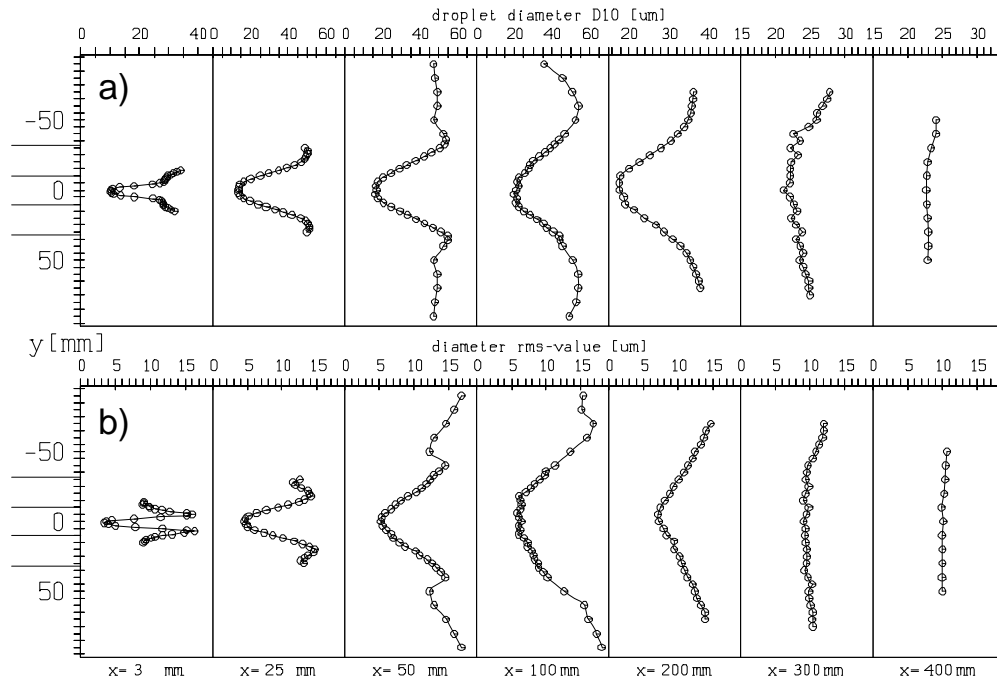


Fig. 11 Profiles of measured droplet number mean diameter (a) and diameter rms-value (b) for case 4 (in μm)

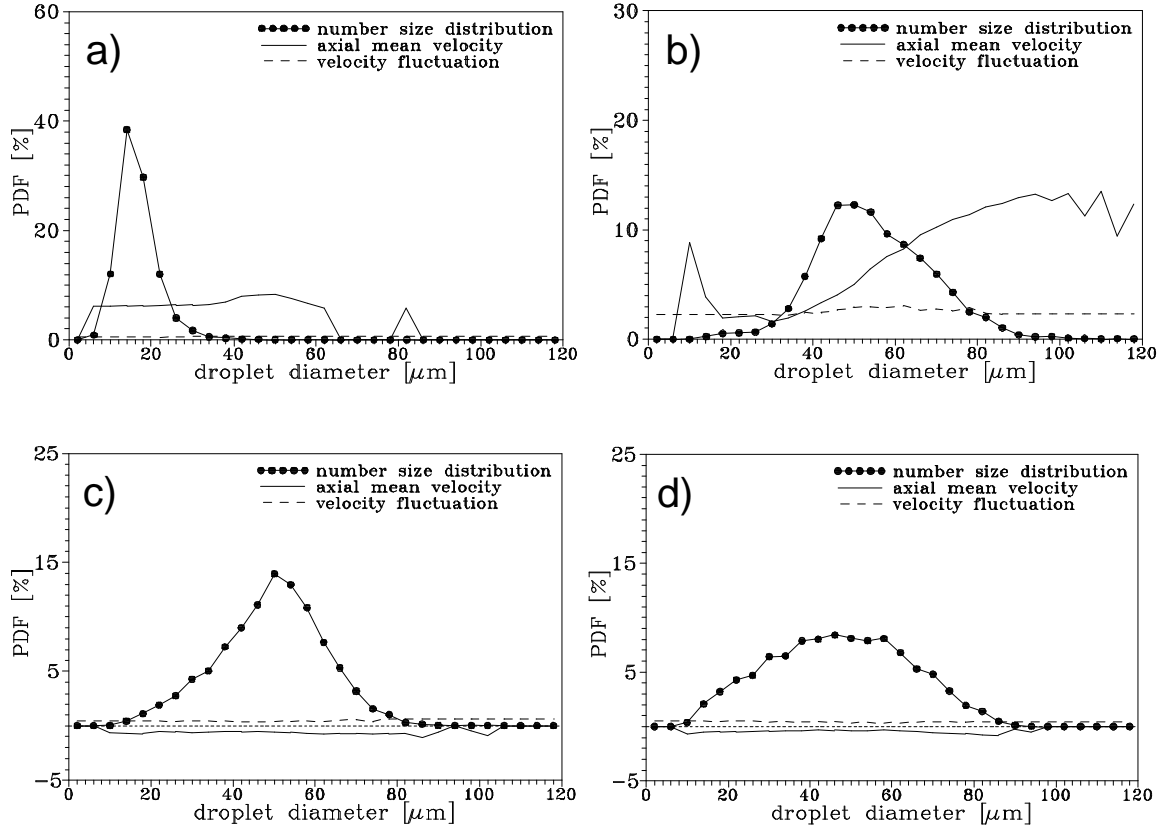


Fig. 12 Droplet size distributions and size-velocity correlations at the cross-section 50 mm downstream the inlet, a) $y = 0$ mm, b) $y = 36$ mm, c) $y = 60$ mm and d) $y = 90$ mm

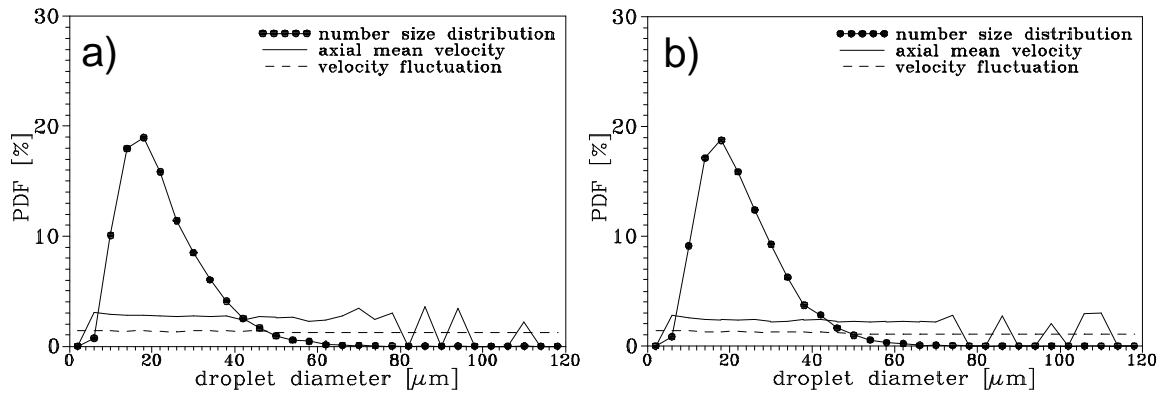


Fig. 13 Droplet size distributions and size-velocity correlations at the cross-section 400 mm downstream the inlet, a) $y = 0$ mm, b) $y = 50$ mm

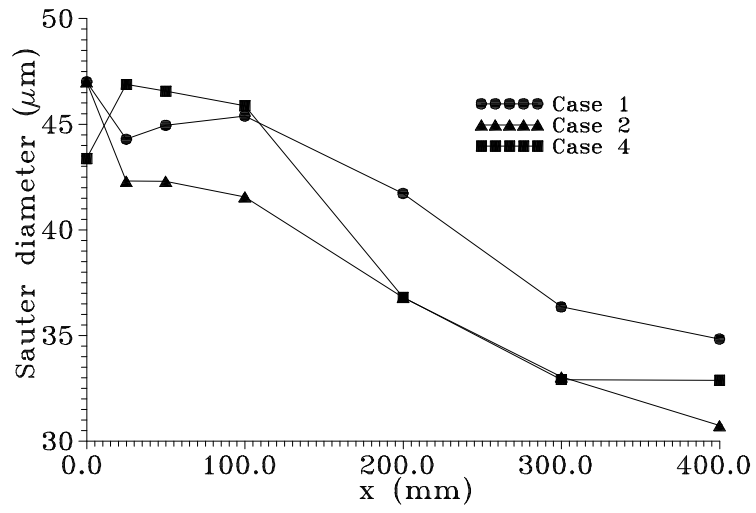


Fig. 14 Averaged Sauter diameter along the test section for cases 1, 2, and 4

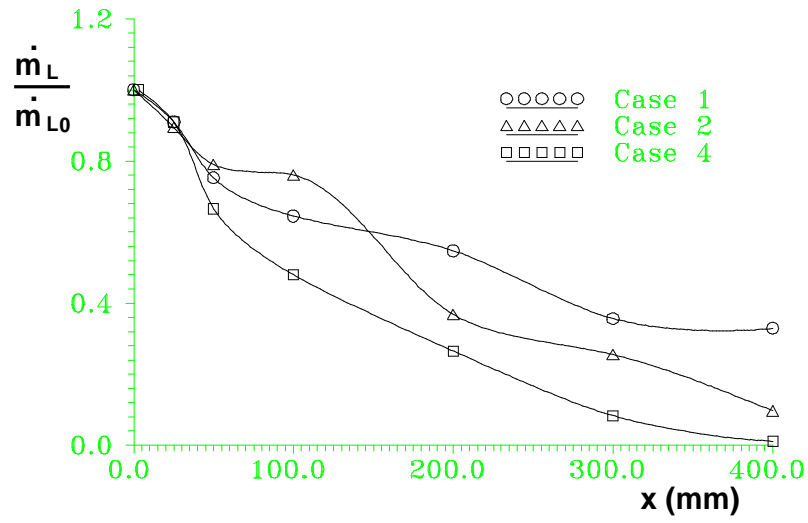


Fig. 15 Droplet mass flow rate along the test section for cases 1,2, and 4

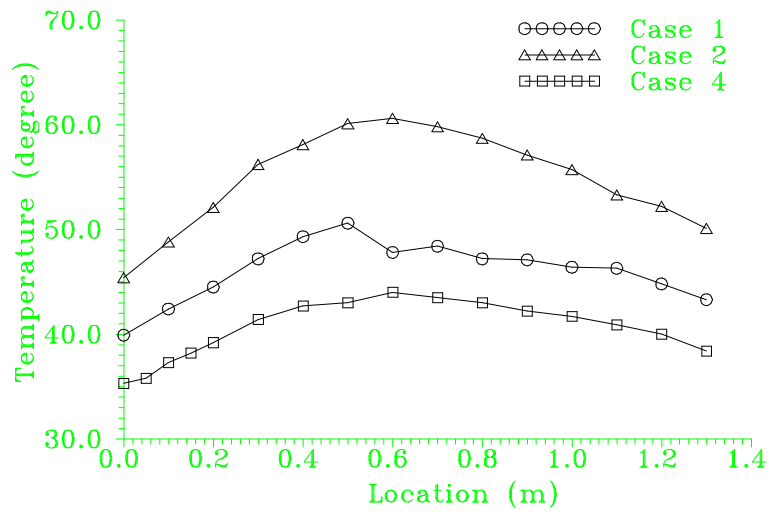


Fig. 16 Temperature distribution along the outer wall of the test section for cases 1, 2, and 4